Journal of Nuclear Materials 381 (2008) 290–296

Contents lists available at ScienceDirect

Journal of Nuclear Materials

journal homepage: www.elsevier.com/locate/jnucmat

Ion beam radiation effects in monazite

V. Picot [a], X. Deschanels [a,*], S. Peuget [b], B. Glorieux [c], A.M. Seydoux-Guillaume [d], R. Wirth [e]

[a] Institut de Chimie Séparative de Marcoule, UMR 5257, BP 17171, 30207 Bagnols-sur-Cèze, France
[b] CEA Centre de Marcoule, BP 17171, 30207 Bagnols-sur-Cèze, France
[c] Laboratoire des Procédés, Matériaux et Énergie Solaire, UPR 8521, Rambla de la Thermodynamique, 66100 Perpignan, France
[d] Laboratoire des Mécanismes et Transferts en Géologie, CNRS, Université Paul Sabatier, IRD, OMP, 14 Avenue Édouard Belin, 31400 Toulouse, France
[e] GeoForschungsZentrum Potsdam, PB 4.1, Telegrafenberg, 14473 Potsdam, Germany

ARTICLE INFO

Article history:
Received 13 February 2008
Accepted 1 September 2008

PACS:
81.05.Je
61.82.−d
61.80.Jh
28.41.Kw

ABSTRACT

Monazite is a potential matrix for conditioning minor actinides arising from spent fuel reprocessing. The matrix behavior under irradiation must be investigated to ensure long-term containment performance. Monazite compounds were irradiated by gold and helium ions to simulate the consequences of alpha decay. This article describes the effects of such irradiation on the structural and macroscopic properties (density and hardness) of monazites $LaPO_4$ and $La_{0.73}Ce_{0.27}PO_4$. Irradiation by gold ions results in major changes in the material properties. At a damage level of 6.7 dpa, monazite exhibits volume expansion of about 8.1%, a 59% drop in hardness, and structure amorphization, although Raman spectroscopy analysis shows that the phosphate–oxygen bond is unaffected. Conversely, no change in the properties of these compounds was observed after He ion implantation. These results indicate that ballistic effects predominate in the studied dose range.

1. Introduction

Monazite compounds have been a subject of particular interest since the 1980s as a potential matrix for conditioning the minor actinides [1,2]. Monazite is a rare earth orthophosphate $Ln^{3+}PO_4$ (where 'Ln' is La to Gd) crystallizing in a monoclinic system (space group $P2_1/n$, Z = 4). It consists of alternating chains of PO_4 tetrahedra and LnO_9 polyhedra. Tetravalent cations can be incorporated with a divalent cation at the lanthanide site. In this case the orthophosphate $Ca^{2+}B^{4+}(PO_4)_2$ is called brabantite by mineralogists, although its crystallographic structure is exactly the same as that of monazite. The solid solution between the pure monazite $Ln^{3+}PO_4$ and brabantite $Ca^{2+}B^{4+}(PO_4)_2$ poles allows simultaneous loading of trivalent and tetravalent cations. Most studies of natural analogs concern ceramics incorporating trivalent lanthanides and tetravalent actinides such as uranium and thorium. These natural monazite–brabantite solid solutions are capable of incorporating actinides in large quantities (up to 15 oxide wt% thorium and 6 oxide wt% of uranium) [3–5]; they exhibit good chemical durability [6] and are never metamict despite sometimes very high integrated doses ($\sim 2 \times 10^{20}$ α/g, i.e., 14 dpa) [7–9], indicating a structure with satisfactory self-irradiation resistance. Experimental studies show that monazite is able to restore its structure at low temperature [10]. The literature includes many publications on synthetic compounds doped with trivalent [11–17] or tetravalent [18–20] actinides, but relatively few papers dealing with compounds incorporating both tri- and tetravalent elements [21]. These studies describe structural modifications (amorphization) and microstructural changes (swelling) in the materials as a result of cumulative irradiation damage arising from alpha decay. Amorphization of $^{238}PuPO_4$ was observed at a dose of 8.6×10^{17} α/g (0.1 dpa), whereas (La, ^{238}Pu)PO_4 remained crystallized after integrated doses of up to 2.5×10^{18} α/g (0.25 dpa) [22]. Moreover, in addition to the amorphization process, a crystal lattice volume increase of about 1.1% was observed in $^{241}AmPO_4$ ceramics after integrating a dose of 8.3×10^{17} α/g (0.1 dpa) [23]. External irradiation has also been used to simulate alpha decay, and shows that monazite can be amorphized by heavy ions (Kr) for damage of less than 2 dpa [24,25]. However, the monazite structure can be easily be restored by annealing at low-temperature (300 °C) [26] or under an electron beam [25–27]. The self-irradiation behavior of monazite combines two opposing phenomena: defect creation by alpha disintegration, and low-temperature annealing capacity for the recrystallization of the structure. This dichotomy is no doubt responsible for the very scattered critical amorphization doses (0.1–2 dpa) reported for this structure in the literature [22–24].

In this article, the underlying mechanisms responsible for the long-term changes of the properties of monazite under irradiation are discussed. This question is also of great interest for geoscientists [28,29]. Because of its high actinide (U and Th) contents, such mineral received intense self-irradiation doses during their

* Corresponding author. Tel.: +33 4 66 79 60 87; fax: +33 4 66 79 76 11.
E-mail address: xavier.deschanels@cea.fr (X. Deschanels).

0022-3115/$ - see front matter © 2008 Elsevier B.V. All rights reserved.
doi:10.1016/j.jnucmat.2008.09.001

geological history. Radiation damage may partially or totally destroy the crystal lattice, dramatically changing their physical and chemical properties [30–32] and modifying the kinetics of resetting. It was, for example, suggested that Pb diffusion is enhanced in a metamict crystal [33] because radiogenic Pb diffuses much faster within 'channels' that correspond to the percolating interface between amorphous and crystalline domains [29–35]. Moreover, radiogenic Pb can be leached more easily from a damaged lattice [36,37]. Consequently, a damaged lattice will retain radiogenic Pb to a lesser degree than a perfect one, resulting in discordant ages for phases that exist in such a structural state. Micro-nano-structural investigations are, therefore, of fundamental importance to better understand isotopic ages of minerals [8–38].

In this study, external irradiation has been used to simulate the consequences of cumulative alpha decay on the structure and properties of monazite. The use of different elements (Au, He) to irradiate the samples allowed us to discriminate between damage caused by the recoil nucleus and by the recoil nucleus and by the alpha particle.

2. Experimental

2.1. Sample preparation

Two rare earth orthophosphates, $LaPO_4$ and $La_{0.73}Ce_{0.27}PO_4$, were prepared by solid-phase reaction according to the protocol described by Montel [39]. This synthesis route involves the following reactions:

$$La_2O_3 + 2NH_4H_2PO_4 \rightarrow 2LaPO_4 + 2NH_3 + 3H_2O \quad (I)$$

$$0.73La_2O_3 + 0.54CeO_2 + 2NH_4H_2PO_4 \rightarrow 2La_{0.73}Ce_{0.27}PO_4 + 2NH_3 + 3H_2O + 0.135O_2 \quad (II)$$

The specific surface area was increased by attrition milling of the precursors and calcined powder samples in a zirconia jar for 2 h at 450 rpm with zirconia beads 1 and 2 mm in diameter (50% of each size), then oven-dried at 100 °C. Pellets were produced by 70 MPa uniaxial press compaction at room temperature, then sintered in air for 4 h at 1450 °C. The geometric density of the sintered pellets was determined by weighing and dimensional measurements (Table 1).

XRD analysis confirmed that the crystallized and monoclinic structure of both compounds studied. No secondary phase was detected using this technique. The measured lattice parameters were consistent with published data (Table 1) [20–40]. Scanning electron microscope examination (Figs. 1 and 2) confirmed that both materials were single-phase compounds.

2.2. Ion beam irradiation

The integrated dose variation versus time after disposal in a monazite–brabantite compound incorporating 10 oxide wt% actinide oxides is shown in Fig. 3.

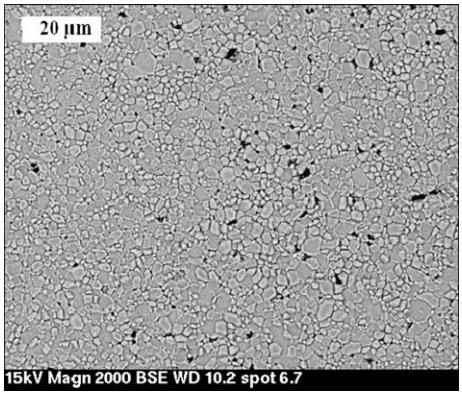

Fig. 1. SEM image of $LaPO_4$ ceramic sintered for 4 h at 1450 °C.

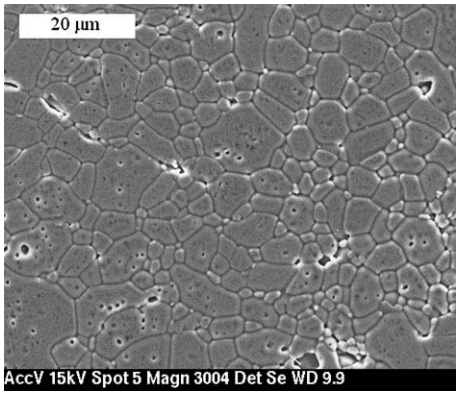

Fig. 2. SEM image of $La_{0.73}Ce_{0.27}PO_4$ ceramic sintered for 4 h at 1450 °C.

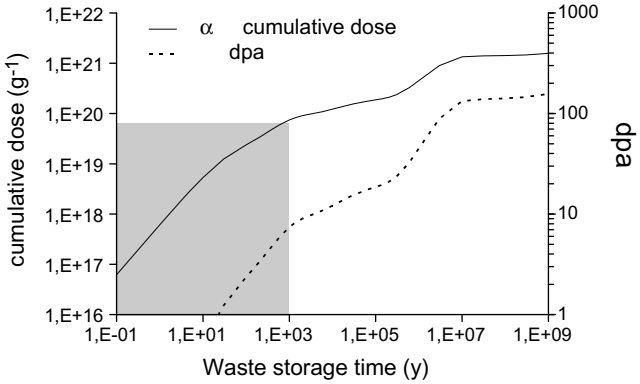

Fig. 3. Integrated dose and number of dpa [41] versus time after disposal of a monazite–brabantite matrix, $La_{0.87}Cm_{0.006}Am_{0.044}Ca_{0.04}Np_{0.04}PO_4$, corresponding to 10 oxide wt% minor actinides in the proportions found in the output flows from reprocessing of the benchmark spent fuel [21]. The shaded zone corresponds to the range simulated by external irradiation.

Table 1
Properties of starting materials

Characteristics	$LaPO_4$	$La_{0.73}Ce_{0.27}PO_4$	$LaPO_4$ from Ref. [20]	$La_{0.73}Ce_{0.27}PO_4$ from Refs. [21,41]
Geometrical density (g cm^{-3})	4.86 ± 0.04	4.73 ± 0.09	–	–
Relative density (%)	95 ± 1	92.5 ± 2	–	–
Crystal parameters				
a (Å)	6.8396(4)	6.8253(8)	6.837	6.824
b (Å)	7.0733(4)	7.0606(8)	7.077	7.061
c (Å)	6.5112(4)	6.4953(5)	6.510	6.498
β (°)	103.288(3)	103.318(5)	103.24	103.29
V (Å^3)	306.57(2)	304.59(3)	306.50	304.68

Alpha decay generates a recoil nucleus with an energy between 70 and 100 keV and a very high-energy alpha particle of about 5 MeV that captures two electrons to produce a helium atom in the structure. The kinetic energy of these particles is deposited in the host material by two distinct processes [30]:

- Ballistic processes corresponding to elastic collisions between atomic nuclei, resulting in atomic displacements; the energy deposited by this process is written E_{nucl}.
- Ionization and electronic excitation processes resulting in a temperature rise in the material and capable under certain conditions of inducing a few atomic displacements; the energy deposited by this process is written E_{elec}.

The energy fractions transferred by the two process for external irradiation and actinide-doped materials are indicated in Table 2. The recoil nucleus has a range of about 40 nm in the material and transfers its energy mainly through ballistic processes, causing many atomic displacements (≈1500 displacements per event). The alpha particle has a range of a few tens of micrometers, transferring virtually all its energy through process ionization and, near the end of its track, a very small fraction in the form of elastic collisions generating about 100 atomic displacements.

To a large extent external irradiation with He and Au ions can be used to simulate energy deposits corresponding, respectively, to the alpha particle and recoil nucleus. In the case of irradiation by helium ions the energy fractions (f_{elec} and f_{nucl}) are practically identical to those of the decay alpha particle, whereas with Au ions the energy fraction deposited by inelastic processes (f_{elec}) is higher (see Table 2). The fluence values were selected to simulate a deposited energy per unit volume comparable to the level after 1000 years in a monazite–brabantite matrix containing 10 oxide wt% minor actinides (Fig. 3). This corresponds to a nuclear damage range between 0.03 and about 7 dpa. The deposited energy per unit volume was calculated on the basis of simulations with SRIM 2003. The implantation was carried out at room temperature at the Orsay Nuclear and Mass Spectrometry Center [43], and the main characteristics are indicated in Table 3.

The ion energy values were selected to damage the material to depths compatible with the characterization tests used in this study (hardness, density, XRD, Raman spectroscopy) and to obtain a deposited nuclear or electronic energy per unit volume that was practically constant throughout the ion penetration depth. Multi-energy Au ion implantation at 1, 3.5 and 7 MeV was used to obtain a constant deposited nuclear energy to a depth of about 1.5 μm; under these conditions the deposited electronic energy was not constant. He ion implantation (1.7 MeV) ensured a constant deposited electronic energy to a depth of 4 μm; in this case damage due to elastic interactions was very limited within the first few micrometers. At the highest He ion fluence levels the He concentration in the implantation peak reached significant values of about 2 at.%.

2.3. Characterization

2.3.1. Density

Density variations in the implanted materials were determined by measuring the irradiation-induced step height on the sample surface. A mask about 200 μm thick with two slits was placed over the sample prior to irradiation. Ion implantation caused swelling or densification of the material, resulting in the appearance of steps at the slit positions. This measurement method is described in detail in Refs. [44,45]. The step height was measured using a Wyko white-light optical interferometer. Given the ion implantation depth, density variations resulting from irradiation can then be determined:

$$\frac{\Delta\rho}{\rho} = \frac{\Delta V}{V} = \frac{100 \times Z}{P}, \tag{3}$$

where Z is the step height in nanometers and P the ion implantation depth in nanometers. The depth corresponds to the x-coordinate of the point at which the nuclear or electronic energy loss (E_{nucl} or E_{elec}) calculated by SRIM 2003 reaches 5% of the plateau value. The volume expansion results obtained by this method are in good agreement with macroscopic swelling measurements of

Table 2
Fraction of initial energy transferred by ionization and electronic excitation (f_{elec}) and by ballistic processes (f_{nucl}) in actinide-doped monazite irradiated externally, based on SRIM 2003 simulations [42]

	$La_{0.87}Cm_{0.006}Am_{0.044}Ca_{0.04}Np_{0.04}PO_4$		Externally irradiated $LaPO_4$	
	Recoil nucleus (100 keV)	Alpha particle (5 MeV)	Au (1, 3.5 and 7 MeV)	He (1.7 MeV)
f_{elec} (%)	39	99.8	74	99.5
f_{nucl} (%)	61	0.2	26	0.5

Table 3
External irradiation characteristics

Fluence (at./cm^2)	F'_1 1.09×10^{15}	F'_2 2.88×10^{15}	F'_3 6.30×10^{15}	F'_4 1.67×10^{16}	F'_5 5.43×10^{16}
He irradiation (1.7 MeV)					
Maximum implanted concentration (ppm)	464	1227	2684	7116	23 137
$E_{nucl} \times 10^{20}$ (keV/cm^3)[a]	0.11	0.29	0.63	1.7	5.4
$E_{elec} \times 10^{20}$ (keV/cm^3)	49	130	280	750	2400

Fluence (at./cm^2)	F_1 9.6×10^{12}	F_2 1.73×10^{13}	F_3 3.8×10^{13}	F_4 9.6×10^{13}	F_5 7.2×10^{14}	F_6 2.3×10^{15}
Au irradiation (1, 3.5 and 7 MeV)						
Maximum implanted concentration (ppm)	2	3	6	16	115	376
$E_{nucl} \times 10^{20}$ (keV/cm^3)	1	1.8	4	11	79	250
$E_{elec} \times 10^{20}$ (keV/cm^3)	2.8	5.1	11	29	220	700
dpa	0.03	0.05	0.11	0.28	2.11	6.7

[a] E_{nucl} was calculated for a mean nuclear damage depth of 2.7 μm as determined by Vickers microindentation.

actinide-doped materials [44], substantiating the validity of this measurement method.

2.3.2. Hardness measurement

The hardness of the monazite matrices was measured by Vickers microindentation on polished specimens implanted with Au and He ions, by applying a 1–5 g load for 15 s at a rate of 0.100 N/s. The microhardness was determined from the following relation:

$$H_v = \frac{2F\sin\left(\frac{136}{2}\right)}{d^2}, \quad (4)$$

where H_v is the Vickers hardness (MPa), F the force applied (N), and d is the mean length of the indentation diagonal (mm). For each characterization the hardness represents the mean of 10 measurements. Based on results shown in Fig. 4, loads of less than 2 and 5 g were used to measure microhardness variations on the samples implanted with gold and helium ions, respectively, so as to indent only the irradiated zone.

2.3.3. XRD measurement

Analyses were carried out using a Philips diffractometer with radiation Cu Kα radiation (λ = 1.5425 Å) using a 0.18 parallel-plate collimator and a sealed proportional detector in the 2θ range from 16° to 50° in 0.02° steps and a counting time of 110 s. The samples were analyzed at grazing incidence to characterize only the irradiation-damaged thickness on the sample surface. Successive measurements determined an incidence angle (2.3°) for which the analysis is characteristic of the irradiated layer (Fig. 5). The lattice parameters were calculated with TOPAS with *hkl*-phase refinement in full-profile matching mode.

2.3.4. Raman measurements

Raman spectra were obtained using a Labram Raman spectrometer and CCD detector coupled with an Olympus optical microscope. The sample was illuminated by a YAG laser beam at a wavelength of 532 nm. A 100× objective and 1800 lines/mm grating were used. The spectra were recorded between 70 cm^{-1} and 1470 cm^{-1} with a spectral resolution of 2 cm^{-1}. The structural data from the outer micrometers at the surface of the irradiated samples were determined by combining confocal Raman microscopy (with an axial resolution of 2 μm) with a motorized *z*-stage to obtain relative band profile variations.

3. Results

3.1. Ion implantation depth

The ion implantation depth estimated from SRIM 2003 simulations was about 1.5 μm in the case of irradiation with gold ions.

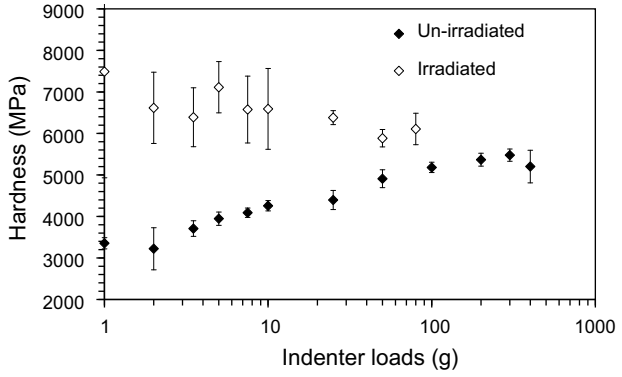

Fig. 4. Vickers hardness variation versus applied load on a pristine monazite $LaPO_4$ implanted with Au ions with a fluence of 2.3×10^{15} at./cm^2.

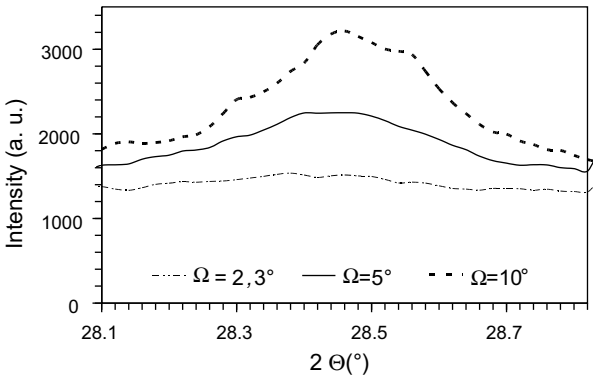

Fig. 5. (1 2 0) Reflection versus incidence angle of monazite $LaPO_4$ irradiated by Au ions at highest fluence.

The estimated value is in close agreement with the value measured by transmission electron microscopy on thin sections obtained by the focused ion beam at the GFZ-Potsdam [46] technique on a $La_{0.73}Ce_{0.27}PO_4$ sample irradiated at the highest fluence (Fig. 6).

3.2. Swelling measurements

Irradiation by Au ions resulted in significant swelling of both ceramic matrices. The swelling saturated at about 8% for an irradiation fluence exceeding 10^{14} at./cm^2. Helium implantation caused slight swelling (about 0.8%) of the $LaPO_4$ matrix (Fig. 7).

3.3. Hardness measurements

Fig. 10 summarizes the hardness values measured on the materials irradiated by gold and helium. The hardness of the materials irradiated by gold ions diminished, stabilizing at about 3000 MPa for a fluence exceeding 10^{14} at./cm^2 (i.e., 10^{21} keV/cm^3). The hardness variation for both monazite matrices was very similar. At the highest fluence F_6 (2.3×10^{15} at./cm^2) a hardness reduction of about 59% compared with the initial value was observed for both monazite matrices. Fig. 10 shows that the hardness of the two matrices irradiated by helium ions did not vary beyond the measurement uncertainty range.

3.4. XRD measurements

The diffraction peaks of monazites $LaPO_4$ gradually disappeared as the gold ion fluence increased. Above the fluence F_4 (9.3×10^{13} at./cm^2), the structure diffraction peaks broadened

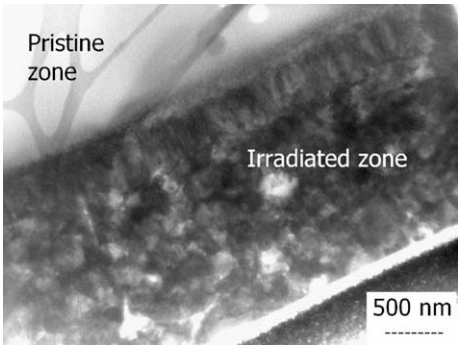

Fig. 6. TEM-BF (bright field) image showing the thickness of the irradiated zone in a monazite $La_{0.73}Ce_{0.27}PO_4$ sample irradiated by gold ions at a fluence of 2.3×10^{15} cm^{-2}. The amorphous zone recrystallized under electron beam.

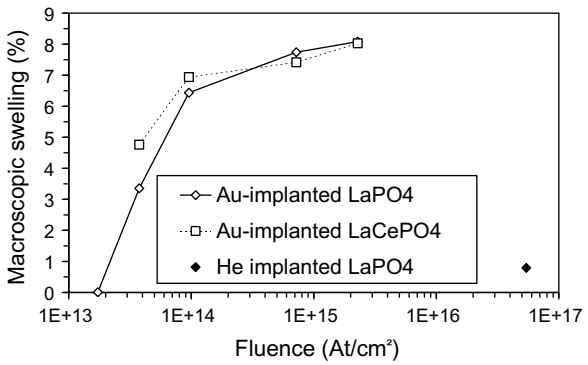

Fig. 7. Volume expansion versus fluence in materials implanted with Au and He ions.

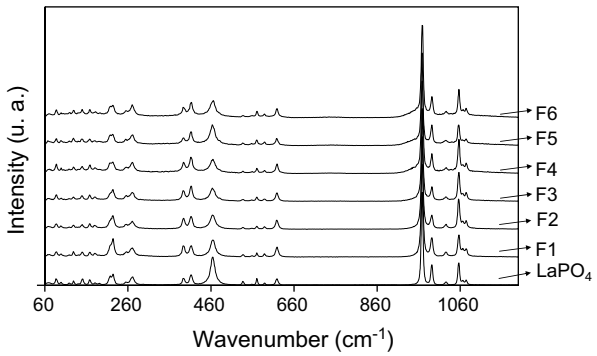

Fig. 8. Raman microspectrometry spectra of pristine and gold-irradiated monazites.

and some reflections disappeared. Amorphization was practically complete at fluence F_5 (7.2×10^{14} at./cm^2). Au ion implantation thus destroyed the long-range crystalline order, whereas irradiation with helium ions had no effect. Table 4 indicates the unit cell volume versus the fluence, and the amorphous fraction for monazites irradiated with gold ions. Broadening of the diffraction peaks above fluence F_1 (9.6×10^{12} at./cm^2) made it impossible to determine the unit cell volume.

3.5. Raman measurements

Raman microspectroscopy analyses were performed on pristine monazite and on gold-irradiated monazite. The signature of the four internal vibration modes of the PO_4^{3-} phosphate group (ν_s between 950 and 1000 cm^{-1}; ν_{as} between 1020 and 1150 cm^{-1}; δ_s between 350 and 450 cm^{-1}; δ_{as} between 560 and 630 cm^{-1} [47]) was effective regardless of the irradiation fluence (Fig. 8).

According to Nasdala [48,49] and Seydoux-Guillaume [7] the loss of short-range order in the zircon compound ($ZrSiO_4$) is apparent in the Raman spectra in the form of broader bands shifted toward lower wave numbers. In our study, despite slight broadening of a few bands attributable to the measurement statistics (ν_s vibration), the peaks can be considered to remain narrow. The phosphate tetrahedra, therefore, do not appear to be affected by irradiation. The existence of these bands even at the highest fluence values when the crystalline order has disappeared shows that the material is not completely damaged. Irradiation with gold ions thus results in amorphization of the crystal lattice (long-range order) but does not locally destroy the PO_4^{3-} polyhedra.

4. Discussion

4.1. Effect of the type of deposited energy on the behavior of monazite

4.1.1. Deposited electronic energy

As noted above, irradiation by helium ions is intended to simulate the impact of electronic interactions. No change in the structure of helium-implanted monazites was observed over the full experimental fluence range. The X-ray diffraction diagrams measured on monazites implanted with helium ions at fluence F_5' (5.43×10^{16} at./cm^2) were comparable to that of unimplanted monazite. Moreover, no significant change was observed in the hardness of the test samples. No monazite swelling was observed for deposited energy values below 7.5×10^{22} keV$_{elec}$/cm^3. Slight swelling, however, less than 0.8%, was observed for the highest fluence corresponding to a deposited electronic energy of 2.8×10^{23} keV$_{elec}$/cm^3. This volume expansion could perhaps be related to helium accumulation, which locally exceeded 2 at.% (Table 3). All these results show that energy losses through electronic interactions resulting from helium implantation do not affect the macroscopic, mechanical, and structural properties of monazite matrices within the experimental fluence range.

4.1.2. Deposited nuclear energy

As noted above, irradiation by gold ions is intended to simulate the impact of nuclear interactions. Gold ion implantation resulted in swelling of the monazite matrices by up to 8.1% at the highest fluence (Fig. 9). Moreover, X-ray diffraction diagrams showed amorphization of the monazite matrices under ion irradiation as the fluence increased. The amorphous fraction and macroscopic swelling (Fig. 9) varied in similar fashion with the deposited nuclear energy. For a deposited nuclear energy level of 10^{21} keV/cm^3, the amorphous monazite fraction exceeded 90% and the structure vol-

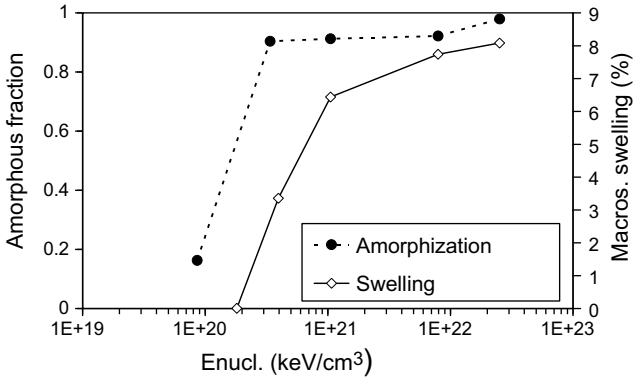

Fig. 9. Amorphous fraction and macroscopic swelling versus E_{nucl} for $LaPO_4$ ceramic.

Table 4
Mesh cell volume versus fluence and normalized area of diffraction peak (120) of $LaPO_4$ monazite compounds irradiated by gold ions

Fluence (at./cm^2)	0	9.6×10^{12}	3.8×10^{13}	9.6×10^{13}	7.2×10^{14}	2.3×10^{15}
V (Å^3)	304.2(5)	304.4(2)	–	–	–	–
$I_{(120)}$ (cps)	1726	1360	180	171	136	69
$f_{amorph} = (I_{(120)} - I_{(120)})/I_{(120)}$	0	0.21	0.895	0.9	0.92	0.96

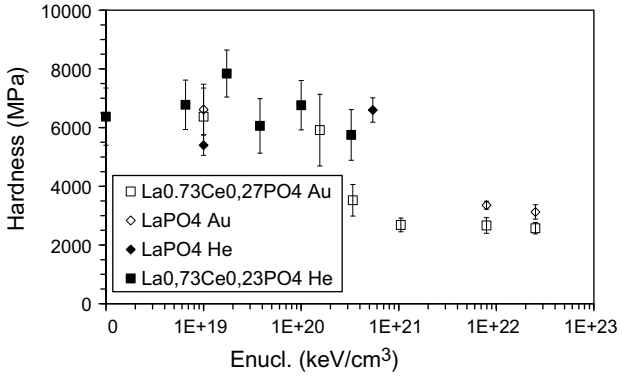

Fig. 10. Hardness variations of materials implanted with Au and He ions versus E_{nucl}.

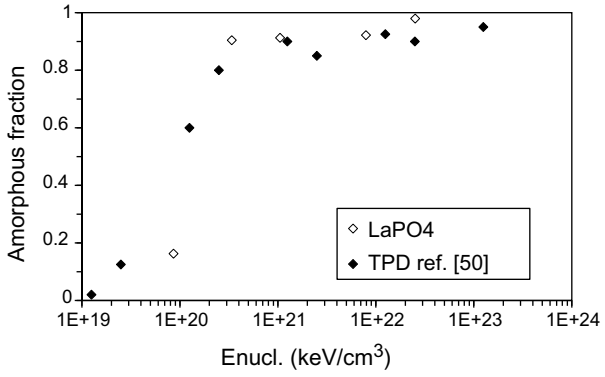

Fig. 11. Comparison of amorphous fraction versus E_{nucl} in $LaPO_4$ and (TPD) $Th_4(PO_4)_4P_2O_7$ ceramics.

ume expansion stabilized. The correlation between these two phenomena indicates that the ballistic processes which generate point defects, and thus amorphization, in monazite are responsible for these changes. This finding suggests another interpretation for the 0.8% volume expansion observed in monazite irradiated by ions He at the highest fluence (Fig. 7), which could be attributable to energy losses through nuclear interactions, which are no longer negligible near the end of the helium particle range.

Finally, the hardness of monazite diminishes by about 59% with the deposited nuclear energy, and once again stabilizes for a deposited nuclear energy exceeding 5×10^{20} keV_{nucl}/cm^3 (Fig. 10). The evolution of this property also appears to be related to the creation of point defects in the structure.

The results obtained show that only nuclear effects result in major modifications of the macroscopic, mechanical, and structural properties of monazite matrices at the tested fluence levels: the deposited nuclear energy (10^{21} keV/cm^3) corresponding to monazite amorphization and stabilization of these properties is the same, and no changes in volume or hardness were observed versus the deposited electronic energy. The same results were obtained for both compositions studied ($LaPO_4$, $La_{0.73}Ce_{0.27}PO_4$).

4.2. Irradiation stability of the phosphate group?

The results of this study showed that the deposited nuclear energy is responsible for amorphization of the monazite compound, but that this parameter does not affect the stability of the phosphate group. The same conclusion was reached by Tamain [50] on thorium phosphate diphosphate compound $Th_4(PO_4)_4P_2O_7$ with phosphate groups. She showed that irradiation by 4 MeV gold ions resulted in amorphization of this structure, whereas – as with monazite – irradiation by helium ions did not lead to structural changes. The variation in the amorphous fraction calculated from diffraction diagrams was comparable to that observed for monazite (Fig. 11).

Only nuclear effects modify the structural properties of $Th_4(PO_4)_4P_2O_7$ compounds at the tested fluence values. Irradiation of the same compounds with 840 MeV Kr ions led to amorphization of the material, but did not damage the P–O chemical bonds [50]. A similar result was also reported for actinide-doped monazites. The Raman spectra of $^{243}AmPO_4$, $^{248}CmPO_4$, $^{249}CfPO_4$, $^{249}BkPO_4$ and $^{253}EsPO_4$ show well-defined bands indicating conservation of the phosphate group [51] whereas $^{241}AmPO_4$ is amorphous for doses of about 8.3×10^{17} α/g [17].

Work with $M_{10}(XO_4)_6Y_2$ phosphosilicates, where $M = Ca^{2+}$, Sr^{2+}, Pb^{2+}, etc., $XO_4 = PO_4^{3-}$, VO_4^{3-}, SiO_4^{4-}, etc., and $Y = F^-$, OH^-, Cl^-, etc., showed greater irradiation sensitivity at higher SiO_4/PO_4 ratios [52]. Studies of natural apatite also showed that minerals with high silicate content are more sensitive to irradiation [53]. Soulet attributes this result to the fact that the phosphate group in the structure favors annealing of the matrix by alpha irradiation [52]. Meldrum [54,55] also reported that MPO_4 phosphate compounds are characterized by lower annealing temperatures and activation energies than $MSiO_4$ silicate compounds; he attributed this difference to P–O bonds, much stronger and shorter than Si–O bonds [24].

5. Conclusion

Two compositions of monazite ($LaPO_4$, $La_{0.73}Ce_{0.27}PO_4$) were irradiated with gold and helium ions to assess the relative effects of the resulting electronic and nuclear interactions. Only nuclear interactions led to major modifications of the matrix properties within the tested fluence range. No significant differences were observed depending on the monazite composition. A damage dose of 6.7 dpa resulted in 8.1% volume expansion, a 59% hardness reduction, and amorphization of the test matrices, although Raman spectroscopy analysis showed that the phosphate groups were not affected. There appear to be two material damage levels, as observed for the phosphate compound $Th_4(PO_4)_4P_2O_7$ irradiated by high-energy ions. The large-scale crystalline order is destroyed, while locally the chemical groups remain intact.

Although monazite become amorphous after Au-ions irradiation corresponding to a deposited nuclear energy of 2×10^{20} keV/cm^3, natural analogs [7–9] and (La, An)PO_4 compounds [22] remain crystallized for an integrated dose of 2×10^{20} α/g and 2.5×10^{18} α/g corresponding respectively to a deposited nuclear energy of 6.8×10^{22} and 8.5×10^{20} keV/cm^3. This apparent contradiction may be explained by the ability of alpha particle to anneal radiation damages. This alpha-annealing recovery process was observed by Ouchani [56] in fluoroapatite sample. A similar ionization-induced annealing process was discussed by Meldrum [25–27] to explain the recovery of the crystallinity of monazite samples after heavy ions and electron irradiation. Alpha-annealing process may also be effective on ^{238}Pu-doped monazite–brabantite matrices ($La^{238}_{1-x-2y}Pu^{+III}_xCa_yTh^{+IV}_yPO_4$). Such materials are currently being investigated in the Atalante DHA laboratory to monitor the effects of alpha decay damage on the physical properties of the matrices.

References

[1] L.A. Boatner, M.M. Abraham, B.C. Sales, Inorg. Chim. Acta 94 (1984) 146.
[2] R.C. Ewing, L.M. Wang, Phosphates as nuclear waste forms, in: M.J. Kohn, J. Rakovan, J.M. Hughes (Eds.), Reviews in Mineralogy and Geochemistry, vol. 48, 2002. p. 673.
[3] C.M. Gramaccioli, T.U. Segalstad, Am. Mineral. 63 (1978) 757.

[4] L.A. Boatner, B.C. Sales, Monazite, radioactive waste forms for the future, in: W. Lutze, R.C. Ewing (Eds.), Radioactive Waste Forms for the Future, 1988. p. 495.
[5] J.-M. Montel, S. Foret, M. Veschambre, C. Nicollet, A. Provost, Chem. Geol. 131 (1996) 37.
[6] E.H. Oelkers, F. Poitrasson, Chem. Geol. 19 (2002) 73.
[7] A.M. Seydoux-Guillaume, R. Wirth, L. Nasdala, M. Gottschalk, J.-M. Montel, W. Heinrich, Phys. Chem. Miner. 29 (2002) 240.
[8] A.M. Seydoux-Guillaume, R. Wirth, A. Deutsch, U. Schärer, Geochim. Cosmochim. Acta 68 (2004) 2517.
[9] A.M. Seydoux-Guillaume, R. Wirth, J. Ingrin, Eur. J. Miner. 19 (2007) 7.
[10] A. Meldrum, L.A. Boatner, R.C. Ewing, Miner. Mag. 64 (2000) 183.
[11] C.W. Bjorklund, J. Am. Chem. Soc. 79 (1958) 6347.
[12] C.E. Bamberger, R.G. Haire, H.E. Hellwege, G.M. Begun, J. Less Common Met. 97 (1984) 349.
[13] A.S. Aloy, E.N. Kovarskaya, T.I. Koltsova, S.E. Samoylov, S.I. Rovnyi, G.M. Medvedev, L.J. Jardine, Radioactive waste management and environmental remediation, in: Proceeding of the Eighth International Conference on Environmental Management, Bruges, Belgium, 2001, pp. 1833–1836.
[14] C. Keller, K.H. Walter, J. Inorg. Nucl. Chem. 27 (1965) 1253.
[15] V.F. Weigel, H. Haug, Radiochim. Acta 4 (1965) 227.
[16] K.L. Kelly, G.W. Beall, J.P. Young, L.A. Boatner, in: E.J. Moore (Ed.), Scientific Basis for Nuclear Waste Management Proceedings 3, Plenum, 1981, p. 189.
[17] D. Bregiroux, R. Belin, P. Valenza, F. Audubert, D. Bernache-Assollant, J. Nucl. Mater. 366 (2007) 52.
[18] A. Tabuteau, M. Pagès, J. Livet, C. Musikas, J. Mater. Sci. Lett. 7 (1988) 1315.
[19] Y. Dusausoy, N.E. Ghermani, R. Podor, M. Cuney, Eur. J. Miner. 8 (1996) 667.
[20] R. Podor, M. Cuney, Am. Mineral. 82 (1997) 765.
[21] X. Deschanels, V. Picot, B. Glorieux, F. Jorion, S. Peuget, D. Roudil, C. Jegou, V. Broudic, J.-N. Cachia, T. Advocat, C. Den Auwer, C. Fillet, J.-P. Coutures, C. Hennig, A. Scheinost, J. Nucl. Mater. 352 (2006) 233.
[22] B.E. Burakov, M.A. Yagovkina, V.M. Garbuzov, A.A. Kitsay, V.A. Zirlin, in: J.M. Hanchar (Ed.), Scientific Basis for Nuclear Waste Management XXVIII, vol. 824, Springer, Berlin, 2004, p. 219.
[23] D. Bregiroux, PhD Thesis, Université de Limoges 16 Novembre 2005.
[24] A. Meldrum, L.A. Boatner, L.M. Wang, R.C. Ewing, Nucl. Instrum. Meth. Phys. Res. B 127&128 (1997) 160.
[25] A. Meldrum, L.A. Boatner, R.C. Ewing, Am. Phys. Soc. B 56 (1997) 13805.
[26] F.G. Karioris, K. Appaji Gowda, L. Cartz, Radiat. Eff. Lett. 58 (1981) 1.
[27] A. Meldrum, L.A. Boatner, R.C. Ewing, J. Mater. Res. 12 (1997) 1816.
[28] J.A. Speer, Actinide orthosilicates, in: P.H. Ribbe (Ed.), Reviews in Mineralogy and Geochemistry, vol. 5, Mineralogical Society of America, Washington DC, 1982. p. 113.
[29] T.M. Harrison, E. Catlos, J.-M. Montel, U–Th–Pb dating of phosphate minerals, in: P.H. Ribbe (Ed.), Reviews in Mineralogy Geochemistry, vol. 48, Mineralogical Society America, Washington DC, 2002. p. 523.
[30] W.J. Weber, R.C. Ewing, C.R.A. Catlow, T.D. de la Rubia, L.W. Hobbs, C. Kinoshita, H.J. Matzke, A.T. Motta, M. Nastasi, E.K.H. Salje, E.R. Vance, S.J. Zinkle, J. Mater. Res. 13 (1998) 1434.
[31] L.W. Hobbs, F.W. Clinard, S.J. Zinkle, R.C. Ewing, J. Nucl. Mater. 216 (1994) 291.
[32] R.C. Ewing, W.J. Weber, F.W. Clinard, Progr. Nucl. Energy 29 (1995) 63.
[33] D.J. Cherniak, Chem. Geol. 110 (1993) 177.
[34] T. Geisler, K. Trachenko, S. Ríos, M.T. Dove, E.K.H. Salje, J. Phys. Condens. Mater. 15 (2003) 597.
[35] K. Trachenko, M.T. Dove, E.K.H. Salje, J. Appl. Phys. 87 (2000) 7702.
[36] D.W. Davis, T.E. Krogh, Chem. Geol. 172 (2000) 41.
[37] R. Romer, Contrib. Mineral. Petrol. 145 (2003) 481.
[38] A.-M. Seydoux-Guillaume, P. Goncalves, R. Wirth, A. Deutsch, Geology 31 (2003) 973.
[39] J.-M. Montel, B. Glorieux, A.M. Seydoux-Guillaume, R. Wirth, J. Phys. Chem. Solids 67 (2006) 2489.
[40] Y. Ni, J.M. Hughes, A.N. Mariano, Am. Mineral. 80 (1995) 21.
[41] G.H. Kinchin, R.S. Pease, Reports Prog. Phys. 18 (1955) 1.
[42] J.F. Ziegler, P. Biersack, The Stopping and Ranges of Ions in Matter, vol. 1, Pergamon Press, New York, 1985.
[43] E. Cottereau, J. Camplan, J. Chaumont, J. Meunier, H. Bernas, Nucl. Instrum. Meth. Phys. Res. B 45 (1990) 293.
[44] S. Peuget, J.-L. Loubet, S. Pavan, S. Henry, C. Peaucelle, V. Picot, X. Deschanels, P. Nivet, in: Proceedings Congress Matériaux, Dijon, France, 2006.
[45] V. Picot, X. Deschanels, S. Peuget, B. Glorieux, C. Fillet, G. Blondiaux, in: Proceedings Congress Matériaux, Dijon, France, 2006.
[46] R. Wirth, Eur. J. Mineral. 16 (2004) 863.
[47] G.M. Begun, G.W. Beall, L.A. Boatner, W.J. Gregor, J. Raman Spectrosc. 11 (1981) 273.
[48] L. Nasdala, D. Wolf, G. Irmer, Eur. J. Miner. 7 (1995) 471.
[49] L. Nasdala, C.L. Lengauer, J.M. Hanchar, A. Kronz, R. Wirth, P. Blanc, A.K. Kennedy, A.M. Seydoux-Guillaume, Chem. Geol. 191 (2002) 121.
[50] C. Tamain, F. Garrido, L. Thome, N. Dacheux, A. Ozgumus, A. Benyagoub, J. Nucl. Mater. 357 (2006) 206.
[51] D.E. Hobart, G.M. Begun, R.G. Haire, H.E. Hellwege, J. Raman Spectrosc. 14 (1983) 59.
[52] S. Soulet, J. Carpéna, J. Chaumont, O. Kaitasov, M.O. Ruault, J.C. Krupa, Nucl. Instrum. Meth. Phys. Res. B 184 (2001) 383.
[53] J. Carpena, J.R. Kienast, K. Ouzegane, C. Jehanno, Geol. Soc. Am. Bull. 100 (1998) 1237.
[54] A. Meldrum, L.W. Wang, R.C. Ewing, Nucl. Instrum. Meth. Phys. Res. B 116 (1996) 220.
[55] A. Meldrum, L.A. Boatner, W.J. Weber, R.C. Ewing, Geochim. Cosmochim. Acta 62 (1998) 2509.
[56] S. Ouchani, J-C Dran, J. Chaumont, Nucl. Instrum. Meth. Phys. Res. B 132 (1997) 447.